# Impact on signal SNR of local ambient noise recorded at the ET candidate sites

Matteo Di Giovanni [1, 2] Davide Rozza [3, 4] Rosario De Rosa,[5, 6] Domenico D'Urso

[7, 8] Luca Naticchioni [2] The Sardinia site characterization team,[9] and others[9]

[1]*La Sapienza Università di Roma, I-00185 Roma, Italy*
[2]*INFN, Sezione di Roma, I-00185 Roma, Italy*
[3]*INFN, sezione di Milano Bicocca, I-20126, Milano, Italy*
[4]*Università di Milano Bicocca, I-20126, Milano, Italy*
[5]*Universitá Federico II Napoli, 80126 Napoli, Italy*
[6]*INFN - sezione di Napoli, 80126 Napoli, Italy*
[7]*Department of Chemistry, Physics, Mathematics and Natural Science,*
*Università degli Studi di Sassari, I-07100, Sassari, Italy*
[8]*INFN, sezione di Cagliari, I-09042, Monserrato (Cagliari), Italy*
[9]*many affiliations*
(Dated: July 8, 2024)

We present an evaluation of how site dependent noise can affect the signal to noise ratio (SNR) of compact binary coalescence (CBC) signals in the future 3rd generation gravitational wave (GW) detector Einstein Telescope (ET). The design of ET is currently pushing the scientific community to study its scientific potential and to assess its sensitivity with respect to known, and possibly unexpected, GW signals using its design sensitivity. Nevertheless, local ambient noise may have an impact on the ET sensitivity at low frequency and therefore affect the SNR of CBC signals at low frequency. Therefore, we study the impact of ambient noise on the ET sensitivity at the two sites candidate to host ET - Sardinia, in Italy, and the Euregio Meuse-Argonne (EMR) between the Netherlands and Belgium - and infer the impact on the ET sensitivity curve and how the SNR of CBC signals at low frequencies is affected. We find that the ambient noise in Sardinia has a low impact on the low frequency ET sensitivity, which is very close to design. On the other hand, the EMR site is strongly affected by local ambient noise.

## I. INTRODUCTION

With the successful exploitation [1–3] of current 2nd generation gravitational wave (GW) detectors, namely Advanced Virgo (AdVirgo), located in Italy [4], Advanced LIGO Hanford and Livingston (aLIGO), located in the United States [5] and KAGRA in Japan [6], the scientific community started to thoroughly investigate [7, 8] the prospects of future 3rd generation GW detectors such as the Einstein Telescope (ET) [9–12], which has been first proposed in 2010 and is expected to be complete by the mid 2030s.

The improvements of ET with respect to current-generation detectors include the extension of the observation bandwidth from the current limit of about $20\,\mathrm{Hz}$ to $2\,\mathrm{Hz}$ and an improvement of the sensitivity by about a factor ten across the band covered by current detectors [12]. Furthermore, ET will be composed of three pairs of nested interferometers arranged in an equilateral triangle (also called xylophone configuration, Figure 1) with the sides $10\,\mathrm{km}$ long. For each interferometer pair, one detector will be optimized for low frequencies ($2\,\mathrm{Hz} < f < 40\,\mathrm{Hz}$) and the other for high frequencies ($f > 40\,\mathrm{Hz}$) [12]. A more classical L-shaped interferometer, like current detectors but with 15 km long arms, is being considered as well [8]. ET will be hosted at a currently planned depth between $200\,\mathrm{m}$ and $300\,\mathrm{m}$ to reduce seismic motion at the input of the suspension system of the mirrors and to reduce the impact of atmospheric disturbances [13].

The extension of the bandwidth to $2\,\mathrm{Hz}$ and the sharp increase in sensitivity will significantly improve the rate of detected events giving the possibility to issue early warnings for the coalescence of compact objects (CBC) several minutes, if not hours depending on the source, before the merger [7, 8, 14–16]. In fact, with respect to current detectors, CBC signals will spend more time in the ET accessible bandwidth, therefore enabling early detection and sky localization. As it was demonstrated by GW170817 [17–20], this is extremely important in the case of binary neutron stars (BNS) mergers. As a matter of fact, joint multimessenger observations with electromagnetic observatories are paramount to exploit the scientific potential of BNS events and shed new light on the internal structure of neutron stars (NS) [7]. In particular, depending on the distance of the source and requiring a signal-to-noise ratio $\geq 12$ and a sky localization smaller than $100\,\mathrm{deg}^2$, ET is expected to be able to send early warnings between 1 and 20 hours before the BNS merger [7]. The release of an early warning increases the chances of detection for the electromagnetic counterparts. Astronomers would be able to point the telescope in the region of the signal to start the monitoring to obtain pre-merger images as well as merger. This enables to detect the early electromagnetic emission, which is fundamental to understand the physics of the engine and the merger remnant [7].

The significant increase in sensitivity below $100\,\mathrm{Hz}$ will also allow for more detailed observations about the merger of intermediate mass black holes (IMBH) [7, 21–23], i.e. black holes (BH) with masses in the
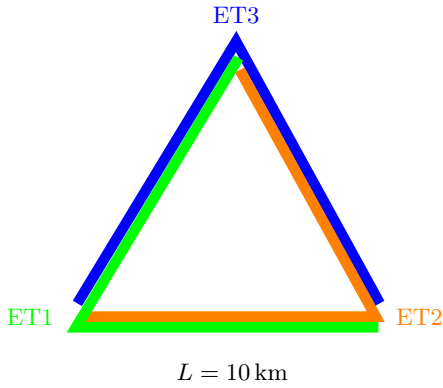
FIG. 1: *Scheme of the ET xylophone for the triangular configuration. Each detector ET1,2,3 is composed of an interferometer optimized for low frequency detection and another optimized for high frequency detection for a total of six.*
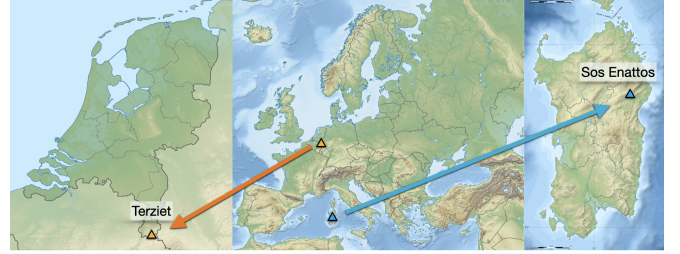


FIG. 2: *Map of Europe showing the locations of the candidate sites to host ET. The village of Terziet in the Netherlands is usually taken as a reference for the EMR candidate site. The maps are taken from [62–64] and modified according to the creative commons license 3.0.*

$[10^2, 10^5] \, \mathrm{M_\odot}$ range. Their typical merger frequency is $< 100 \, \mathrm{Hz}$ and are expected to spend a maximum of $\mathcal{O}(100 \, \mathrm{s})$ in the ET bandwidth. Currently, GW detectors are limited to BH masses $\mathcal{O}(100 \, \mathrm{M_\odot})$ and hypothetical IMBH merger signals are typically only detectable in very short time intervals of a few milliseconds. On the other hand, ET will open the possibility of detecting these IMBH, studying the possibility that they are the seeds of the supermassive BHs in the center of galaxies [7, 23]. Furthermore, a precise reconstruction of waveforms for compact objects during inspiral and merger will allow accurate tests of General Relativity (GR).

Therefore, any degradation with respect to design in the low frequency sensitivity of ET may significantly hinder the capability of early detections and multimessenger observations for BNS mergers and may reduce the quality of the observations for IMBH [8, 15]. As a consequence, since seismic disturbances, of both natural [24–36] and anthropogenic [28, 30, 35, 37–39] origin, are the main source of noise limiting the detector sensitivity at low frequency and can affect GW data in many ways [30, 35, 40–49], seismic characterization studies at the candidate sites to host GW detectors are paramount.

Therefore, the aforementioned improvements of ET with respect to current detectors make a careful assessment of seismic noise at the candidate sites for ET even more important. The goal is to guarantee a suitable environment for this future detector that would make possible the reaching of its design sensitivity [50]. As of 2024, there are two sites which are candidate to host ET (Figure 2): the Euregio Meuse-Rhine (EMR) [11, 12], between Belgium and the Netherlands, and the area surrounding the Sos Enattos former mine in Sardinia (Italy) [11, 12, 51–54].

Since 2014, the Sos Enattos [51–56] and EMR [57–59] sites have been the subject of characterization studies aimed at assessing their suitability to host ET. Nevertheless, except [55] and the recent work published by [60], no works are assessing the impact of site dependent noise on the detectability of GW sources. Therefore, the scope of this paper is to provide a first estimation of how site dependent low frequency noise may affect the signal to noise ratio (SNR) of CBC sources, without entering the details on how parameters estimation would be affected. This aspect is beyond the goal of this work, but may represent its future development. Extending the methodology already shown in [55] and [61], we investigate the case of IMBH and BNS focusing on the $[2, 10] \, \mathrm{Hz}$ range, where ambient noise is more prominent [53–55] and may affect early warnings. First, we use the ET design sensitivity curve as a benchmark and then the modified sensitivity curves according to the actual seismic noise measured at each candidate site.

The paper is organized in the following way: in Section II we discuss the astrophysical background of this study; the method is presented in Section III; Section IV talks through the data used for this study; finally, the results are discussed in Section V and VI, whereas the conclusions are debated in Section VII.

## II. ASTROPHYSICAL BACKGROUND

For a long time, scientists questioned about the existence of a class of black holes (BH), identified as IMBH [21–23], between those formed by stellar collapse (i.e. $M < 10^2 \mathrm{M_\odot}$) and the supermassive BH at the centers of galaxies (i.e. $M > 10^5 \mathrm{M_\odot}$). Before the third observing run (O3) [65] of aLIGO and adVirgo, there was no clear evidence about their existence and the gap between $[10^2, 10^5] \mathrm{M_\odot}$ remained unexplained. During O3, GW190521 [66], consistent with two BH merging to form a $\simeq 140 \mathrm{M_\odot}$ remnant, provided the first direct evidence of IMBH formation. During the same observing run, a

few more marginal candidates for IMBH formation were found, but none sufficiently significant to indicate detection of further IMBH mergers [65, 67]. Their formation channel has not been completely established. A possible explanation is that they may have formed via the subsequent, usually referred to as hierarchical, mergers of lighter BH [68]. Other IMBH formation channels also include the direct collapse of massive first-generation, low-metallicity Population III stars [23]. The existence of IMBH and their accretion through hierarchical mergers may also provide relevant information about the formation of supermassive BH [65].

Since the merger frequency of two compact objects orbiting around each other is inversely proportional to their chirp mass $M_c \equiv \frac{(m_1 m_2)^{3/5}}{(m_1+m_2)^{1/5}}$ as $f_{GW} \propto M_c^{-5/8}$, IMBH merge at relatively low frequencies, i.e. $f < 100$ Hz. For example, using the Keplerian approximation for circular orbits and considering the two BH as merged when their orbital separation is less than the Schwarzschild radius

$$R_s = \frac{2Gm}{c^3},\tag{1}$$

an equal mass IMBH with $m_1 = m_2 = 100 M_\odot$, each with $R_s \simeq 533$km, has an orbital frequency at merger [69]

$$\omega_k(R_s) = \sqrt{\frac{Gm_{tot}}{R_s^3}} \simeq 420\text{Hz}.\tag{2}$$

Which gives an approximate merger frequency

$$f_{GW} = \frac{\omega_{GW}}{2\pi} = \frac{\omega_k}{\pi} \simeq 133\,\text{Hz}.\tag{3}$$

Furthermore, if we calculate the number of cycles spent in a given frequency band $[f_{min}, f_{max}]$ [69]

$$\mathcal{N}_{cyc} = \frac{1}{32\pi^{8/3}} \left(\frac{GM_c}{c^3}\right)^{-5/3} (f_{min}^{-5/3} - f_{max}^{-5/3})\tag{4}$$

we find that most of the cycles of the observable waveform are contained in $[2, 10]$ Hz. At cosmological distances within the reach of ET [7], redshift $z$ also contributes to lowering the observed merger frequency as masses observed on Earth in the detector frame have to be corrected as $m_{det} = m_{sour}(1 + z)$.

Figure 3a shows the time-frequency evolution of an equal mass $m_{tot} = 200\,\text{M}_\odot$ IMBH in the circular orbit, non spinning case computed using the IMRPhenomD waveform approximant [70, 71]. In this case, the merger frequency appears to be $f_{merge} \simeq 82$ Hz, lower than what is shown in Equation 3. This is due to the fact that GW waveform approximants take into account relativistic effects close to the merger. In fact, we refer to the innermost stable circular orbit (ISCO) as the last orbit beyond which stable circular orbits are no longer allowed. For the case mentioned above, $f_{ISCO} \simeq 11$Hz. In particular, IMRPhenomD is based on a combination of analytic post-Newtonian (PN) and effective-one-body (EOB) methods
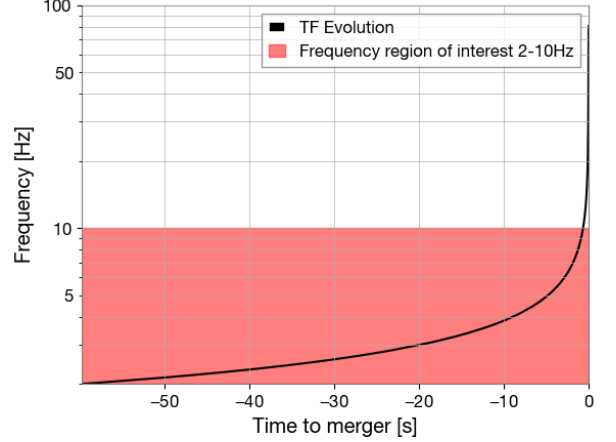


(a) *Time-frequency evolution of an equal mass IMBH with $m_{tot} = 200\,\text{M}_\odot$ in the circular orbit, non spinning case simulated using the IMRPhenomD waveform approximant [70, 71].*
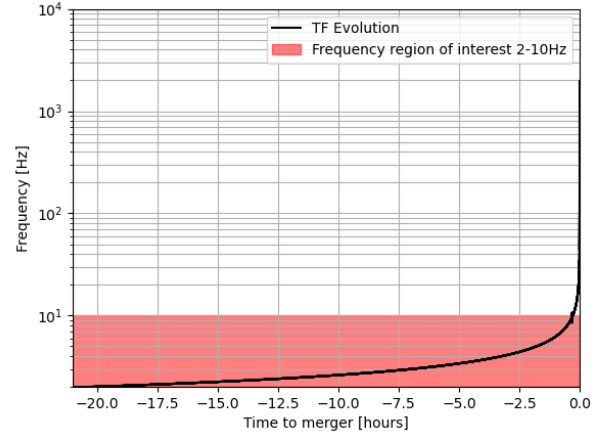


(b) *Time-frequency evolution of an equal mass BNS with $m_{tot} = 2.8\,\text{M}_\odot$ in the circular orbit, non spinning case simulated using the IMRPhenomPv2_NRTidalv2 waveform approximant [72].*

FIG. 3: Time-frequency evolution.

to describe the inspiral, whereas the merger phase is calibrated using numerical relativity models [70, 71]. Figure 3a also highlights the importance of the $[2, 10]$ Hz band, in which an IMBH spends most of the time before the merger.

BNS, on the other hand, are a completely different source. They are composed of two NS, have an expected total mass between $2.2\text{M}_\odot$ and $4.4\text{M}_\odot$ and merge at frequency $\mathcal{O}(\text{kHz})$. All the relevant information carried by GW about the physics of NS can be found in the high frequency part of the signal as well. Nevertheless, low frequency detection plays a crucial role in the observation of BNS mergers. In fact, as men-

tioned in Section I, detecting a BNS as soon as possible may not only significantly increase the observation rate [8, 15, 73], but also allow for precise sky localization [16] and sending prompt early warnings to observatories for conducting multimessengers observing campaigns [7, 14]. Moreover, BNS typically spend several hours at low frequency accumulating SNR before the chirp. Figure 3b shows the time-frequency evolution of an equal mass $m_{tot} = 2.8 \, \mathrm{M}_\odot$ BNS underlining the fact that it spends $\simeq 20 \, \mathrm{hours}$ in the $[2, 10] \, \mathrm{Hz}$ band. Furthermore, Equation 4 shows that $\mathcal{N}_{cyc}([2, 10] \, \mathrm{Hz}) \simeq 7 \times 10^5$ and $\mathcal{N}_{cyc}([2, 4096] \, \mathrm{Hz}) \simeq 7.6 \times 10^5$. This means that only fully accomplishing the low frequency design sensitivity, especially below 10 Hz, may allow to exploit the potential of ET for what concerns multimessenger astronomy [8, 15].

## III.  METHODOLOGY

To estimate the impact of site-dependent noise over the SNR of CBC events, we have to first calculate how site noise changes the ET design sensitivity curve. For this study we use the design curve already applied for [8]. At different frequencies, different contributions affect the ET noise budget curve like seismic, Newtonian, thermal, and quantum noise. Among these noise sources, the highest contribution in the frequency region between 2 and 10 Hz is the Newtonian noise (NN) [49, 74]. NN is caused by gravity fluctuations from masses that are moving around the detector. These fluctuations are generated by variations of atmospheric and ground densities in the vicinity of the test masses of the detectors. Ground density variations are caused by ground motion, i.e. seismic waves; In this work, we focus on NN from the seismic contribution evaluating the Power Spectral Density (PSD) over a given time window. Atmospheric NN is not taken into account due to the current lack of dedicated environmental sensors installed at the ET candidate sites.

The NN projection, already proposed in [55] following [61], can be computed using the following equation:

$$\tilde{h}_{NN}(f) = \frac{4\pi}{3} G \rho_0 \frac{2\sqrt{2}}{L} \frac{1}{(2\pi f)^2} \tilde{x}(f) \qquad (5)$$

where the frequency $(f)$ dependence of the Newtonian noise budget $(\tilde{h}_{NN})$ is related to the gravitational constant $(G)$, the density of the ground medium $(\rho_0)$, the size of the arm-length of each interferometer $(L)$ and the Amplitude Spectral Density (ASD - square root of the PSD) of the seismic displacement $(\tilde{x})$. Equation (5) is evaluated assuming body waves contribution only (surface waves are negligible at a depth of a few hundred meters underground), one-third of contribution to seismic noise is coming from compressional waves, approximated spherical underground cavities for the detector and uncorrelated NN on the interferometer test masses. Equation (5) provides a credible lower limit for NN [74]. The

used ASDs $\tilde{x}$ are the percentiles (10th, 50th, and 90th) of the spectral distributions calculated on $120 \, \mathrm{s}$ windows for the vertical and horizontal channels of the seismometers. The length of the time window is chosen according to the typical maximum duration of an IMBH signal (Figure 5b) and on the time segment duration proposed for CBC multiband analysis for BNS [16]. Under these assumptions, the ET noise budget that we use takes into account the NN evaluated from the seismic noise of each candidate site for the 10th, 50th, and 90th percentile of seismic spectra. Since a simple projection alone does not show the effect of non-stationarity of NN (Glitchness), we also use a more effective indicator, called the Noise to Target Ratio (NTR) and derived from [55]:

$$NTR = \sqrt{\frac{1}{\Delta f} \int_{f_1}^{f_2} df \, \frac{S_n(f)}{S_{n,ET}(f)}} \qquad (6)$$

where the $S_{n,ET}(f)$ is the PSD of the ET design sensitivity, whereas $S_n(f)$ is the PSD of the modified ET sensitivity where the NN was substituted with the contribution of the local noise over the time window decided and $\Delta f = f_2 - f_1$ is the selected bandwidth. In this way, the NTR is evaluated time by time and normalised for the comparison of the two candidate sites.

After inferring the modified ET sensitivity curves, we gather the events of interest for our study from astrophysical catalogs and we use PyCBC [75] to generate and inject signals in simulated ET noise. Waveforms are generated using the IMRPhenomD [70, 71] GW approximant for IMBH and IMRPhenomPv2_NRTidalv2 [72] for BNS, both available in the LIGO-Virgo-KAGRA Algorithm Library (LAL) [76]. To take into account the antenna pattern of the detector, ET is simulated considering three misaligned L-shaped co-located detectors, with an arm length of 10 km and an arm angle of $60°$. Since the actual orientation of the ET triangle has not been decided yet, we choose an arbitrary positioning of the detector. For the Sardinia candidate site, ET is assumed to be located at the Sos Enattos mine at $[40.44°\,\mathrm{N}, 9.44°\,\mathrm{E}]$, whereas for the EMR site, we have chosen the village of Terziet at $[50.73°\,\mathrm{N}, 5.91°\,\mathrm{E}]$ as a reference. For each detector, noise is obtained by generating white noise colored according to the given sensitivity curve and the same sources are taken into account. Waveforms are injected into the noise of each detector composing ET (labeled ET1, ET2 and ET3 respectively).

First, we infer the distribution of the SNR of the signals injected in noise obtained after the ET design sensitivity. Signal SNR is calculated as

$$SNR = \sqrt{MSNR_{ET1}^2 + MSNR_{ET2}^2 + MSNR_{ET3}^2}, \qquad (7)$$

where $MSNR_{ET1,2,3}$ are the matched filter SNR (MSNR) calculated in each detector. Then, using the same events, we repeat the procedure for each curve inferred from Equation 5 using the 10th, 50th and 90th percentile seismic spectra. The new SNR distributions are then com-

pared against the design case used as a benchmark. The distributions of the SNR losses are obtained after calculating, for each event, the ratio between the new SNR and the benchmark SNR. The MSNR is calculated as [77]:

$$MSNR^2(t) = \frac{(s|h_{cos})^2 + (s|h_{sin})^2}{(h_{cos}|h_{cos})} \qquad (8)$$

with

$$(s|h)(t) = 4\mathrm{Re}\int_{f_{min}}^{f_{max}} \frac{\tilde{s}(f)\tilde{h}^*(f)}{S_n(f)}e^{2\pi i f t}df \qquad (9)$$

where $\tilde{s}(f)$ is the Fourier Transform (FT) of the data, $\tilde{h}^*(f)$ is the FT of the template and $h_{cos}/h_{sin}$ are the two orthogonal phase components of the signal, respectively. In our case, $f_{min} = 2\,\mathrm{Hz}$ and $f_{max} = 10\,\mathrm{Hz}$. Since the ET sensitivities are modified only in the $[2, 10]\,\mathrm{Hz}$ range, taking into account Equations 8 and 9 we note that MSNR out of this bandwidth gives the same contribution to the total MSNR in all cases. Therefore we restrict the calculation between 2 Hz and 10 Hz only. It should be pointed out that we also assume perfect knowledge of the source, i.e. matched filter is calculated using the same waveform template injected in the data.

## IV. DATA

### A. Seismic

Seismic data from the candidate sites come from a set of instruments installed to assess the quality of the sites and for site characterization studies. In particular, data from the Sardinia site come from two seismometers installed in boreholes at $\sim -264$ m and $\sim -252$ m at the two proposed vertex locations for the ET triangle known as P2 and P3. The seismometers are Trillium 120 SPH2 coupled with a Nanometrics Centaur CTR4-6S, 6-ch 24-bit data logger. On the other hand, the EMR site is provided with a borehole seismometer, referred to as TERZ, at $\sim -250$ m and equipped with a Streckeisen STS-5A seismometer. In both cases, the time period used for the analysis covers two years, from December 21$^{st}$, 2021 to December 20$^{th}$, 2023. This period of 730 days has a duty cycle $> 90\%$ at both sites. As mentioned above, the PSD time window is 120 s and the percentiles (10th, 50th, and 90th) for each station are evaluated for all three orthogonal channels (the two horizontal components and the vertical one). Data from P3 shows a lower noise level with respect to P2 in all the channels by an average factor of around 20% between 1 and 10 Hz. For this reason, we will compare P2 and TERZ.

Figure (4) shows the comparison of the percentiles of e.g. the vertical component for P2 (in blue) and TERZ (in red) with respect to the Peterson New Low and High Noise Model (NLNM in black dashed line and NHNM in black dotted line respectively) [78]. Above 6 Hz, the P2 data lie on the self-noise of the sensor, making apparent
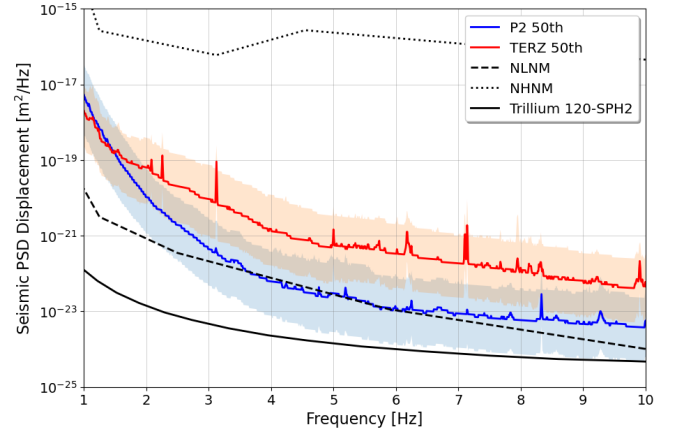


FIG. 4: *Seismic PSD displacement for the two candidate sites, P2 in blue and TERZ in red, is reported as a percentile (50th in solid line while 10th and 90th the lower and upper limit of the colored band). Peterson limits (NLNM in black dashed line and NHNM in black dotted line) and the self-noise of the Sardinian sensor (solid black line) are also shown.*

the quietness of the site. We will use these data in Section V as input parameters for the determination of the ET sensitivity curve.

### B. Astrophysical Sources

The parameters for IMBH and BNS mergers are taken from the catalog [79] used to produce the results of [8], which considers a set of sources spanning one year between the mock dates 01-01-2030 and 12-31-2030. For what concerns BBH, the catalog results from the mixture of BBH from isolated binary evolution, dynamical formation in young, globular and nuclear star clusters. Masses, spins, redshifts and luminosity distances have been obtained with the open-source code FASTCLUSTER [80]. For this work, we select a subset of events, for a total of $\simeq 1 \times 10^3$, that include:

- BBH with at least one source frame component mass above 100 $M_\odot$;

- BBH with both source frame component mass above 100 $M_\odot$;

- BBH with a total mass above 100 $M_\odot$.

Figure 5a shows the distribution of the time to the merger at 10 Hz for these events. We note that once left the frequency band considered in this work, most events have less than 0.5 s before merging. On the other hand Figure 5b shows the time spent in the $[2, 10]\,\mathrm{Hz}$ range and points out how most of the time IMBH lie in this bandwidth before the merger.

For BNS mergers, the source frame masses of the two objects are sampled uniformly in the interval
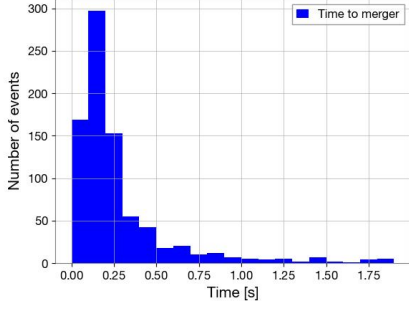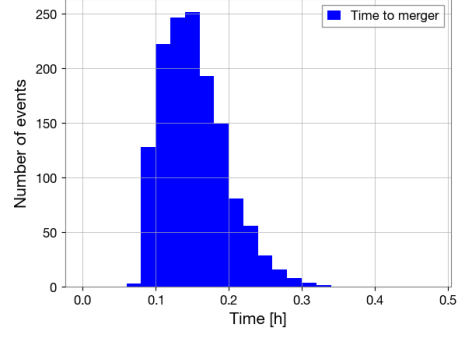
(a) *Distribution of the time to merger at* 10 Hz *for the BBH events considered in this work.*
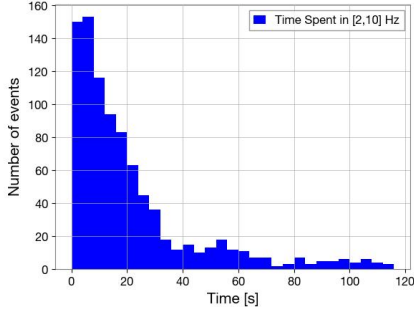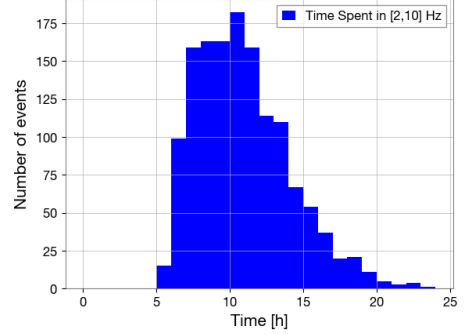


(b) *Distribution of the time spent in the* [2, 10] Hz *range for the BBH events considered in this work.*

FIG. 5: Times distributions for the IMBH of this work.



(a) *Distribution of the time to merger at* 10 Hz *for the BNS events considered in this work.*



(b) *Distribution of the time spent in the* [2, 10] Hz *range for the BNS events considered in this work.*

FIG. 6: Times distributions for the BNS of this work.

[1.1; 2.5]M$_\odot$ so that $m_1 > m_2$. Redshifts and luminosity distances are taken from [81]. As for BBH, we limit ourselves to a subset of events. Since we are not interested in determining the cosmological range at which we can observe these events, but only how signal SNR is affected in the low frequency regime for early warning purposes, we choose mergers at $z < 0.25$ for a total of $\simeq 1.5 \times 10^3$ events. At this range, the BNS signal should reach $SNR \geq 12$ to issue an early warning between 20 hours and 1 hour before the merger. Figure 6a shows the distribution of the time to the merger at 10 Hz for the selected BNS events. We note that once left the frequency band considered in this work, most events have less than 20 min before merger. Figure 6b shows the time spent in the [2, 10] Hz range. The relevance of this bandwidth is apparent, since several hours are spent here.

For both IMBH and BNS, the sky position and coalescence phase are sampled uniformly in the entire sky and between $[0, 2\pi]$, respectively. The inclination angle is sampled from a uniform distribution between $[-\pi, \pi]$ and the polarization angle is sampled uniformly in the interval $[0, \pi]$. For simplicity, we are not considering spins and eccentricity of the orbit assuming the circular orbit non spinning case. Moreover, to take redshift into account, source frame masses are converted into the de-

tector frame as $m_{det} = m_{sour}(1 + z)$.

## V. MODIFIED ET CURVES

The ET sensitivity, modified according to Section III, takes into account the local seismic component of the NN of the two candidate sites. In equation (5) we assume $\rho_0 = 2.7 \cdot 10^3$ kg/m$^3$ and $L = 10$ km. Figure 7 reports the sensitivity curve using the seismic percentiles of P2 (in blue) and TERZ (in red), evaluated in Section IV A, compared with the ET design noise budget (in black) as reported in [8] for the frequency range between 1 Hz and 100 Hz.

To quantify the modified ET sensitivity with respect to the designed one, we evaluated the NTR index defined in Sec. III. While Fig. 7 shows the level of the NN inside the ET sensitivity averaged over two years, the NTR, computed every 120 s, gives information on how many times we are close or far to the ET design curve, i.e., looking to the glitchiness of the site. Focusing our attention on the frequency range between $f_1 = 2$ Hz and $f_2 = 10$ Hz, a value of NTR larger than one implies that, in the selected dataset, the contribution of the NN is limiting the ET sensitivity. The higher the NTR, the
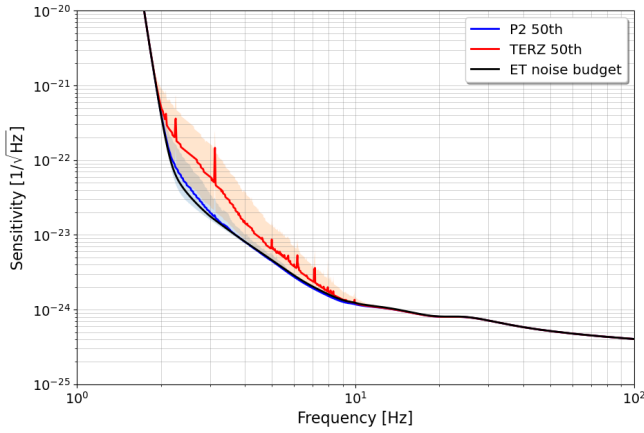
FIG. 7: *Sensitivity curves for the two candidate sites, reporting the percentile (50th in solid line while 10th and 90th the lower and upper limit of the colored band) for P2 (in blue) and TERZ (in red), compared with the ET design sensitivity (black).*
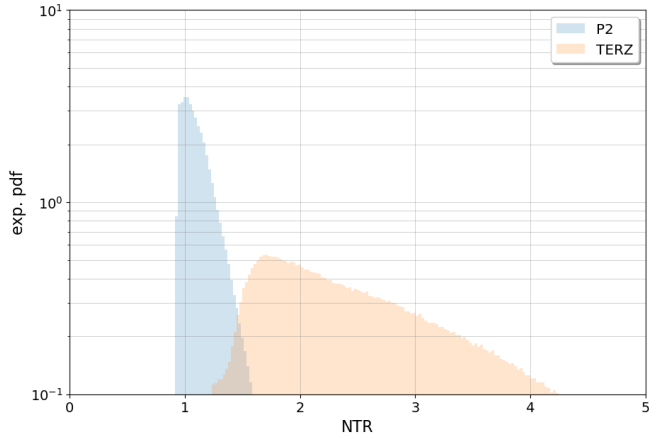


FIG. 8: *NTR normalised distribution for the two sites: P2 (in blue) and TERZ (in red).*

higher the probability of losing the GW signals. One has to remember that if the bandwidth of the GW signal is larger than $f_2$ it is possible to recover the signal since the NN is not significant at higher frequencies.

Figure 8 reports the normalised NTR distribution for P2 (in blue) and TERZ (in red). It is possible to note that P2 is characterised by a lower noise and the majority of the data are distributed around $NTR = 1$. To empathise the difference, we evaluated the cumulative density function (or CDF) of the two distributions. The x-axis of Fig. (9) is the NTR and the y-axis represents the CDF confined between 0 (no data are below the specific NTR) and 1 (all data are below that specific NTR). We reported in Table I the value of the NTR corresponding to the specific percentile for the two sites and in different time periods. The first set of data regards the whole period of two years, 90% of the P2 data are below $NTR = 1.31$, while the same amount of data for
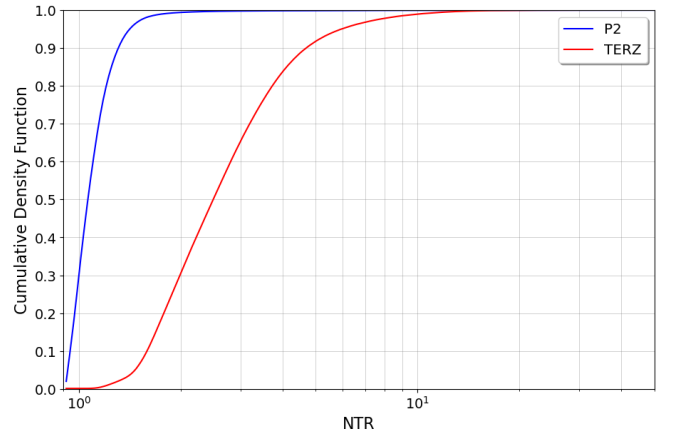


FIG. 9: *Normalised cumulative density function of the NTR normalised distribution, of Fig. 8, for the two sites: P2 (in blue) and TERZ (in red).*

TERZ are below $NTR = 4.69$. We performed the analysis separating working days and weekends, day and night hours. The noise is less on both weekends and nights giving information on the anthropogenic origin of this noise related to human activities. Moreover, this human noise is affecting more the TERZ site, while for P2 the variation is less significant.

## VI. IMPACT ON SIGNAL TO NOISE RATIO

### A. Intermediate Mass Black Holes

Figures 10 and 11 show the SNR distributions for the IMBH case for the Sardinia and EMR candidate sites, respectively. The benchmark SNR distribution inferred using the design ET sensitivity curve is shown in green. The results are also summarized in Table II. In both cases, we analyze the same 970 events. For the Sardinia site, 110 events ($\simeq 11\%$) are below the detectability threshold of $SNR = 12$ [7] already in the benchmark case. The case of Sardinia (Figures 10) shows performances which are mostly on par, if not slightly better, with the benchmark. In the 10th and 50th percentile case, only 92 and 94 events ($\simeq 9\%$) have $SNR \leq 12$. On average, the SNR shows a gain of $\simeq 6\%$ and $\simeq 5\%$, respectively. For the 90th percentile, the number of events below the detectability threshold is 114 making, even in the worst case scenario, the average SNR loss with respect to design marginal ($\simeq 2.5\%$).

For the EMR site, the situation is different. In this case, the benchmark case shows 119 ($\simeq 11\%$) events with $SNR \leq 12$. The slight difference with respect to Sardinia is mainly due to the different location of the detector on the Earth's surface that, for the same coordinates of the sources, changes the detector response to a given position in the sky. We note that the 10th percentile case is on par with the benchmark, with 111 events below

| Percentile | Whole Period | | Working days | | Weekends | | Days | | Nights | |
|---|---|---|---|---|---|---|---|---|---|---|
| | P2 | TERZ | P2 | TERZ | P2 | TERZ | P2 | TERZ | P2 | TERZ |
| 10th | 0.94 | 1.59 | 0.94 | 1.66 | 0.94 | 1.49 | 0.96 | 1.84 | 0.93 | 1.44 |
| 50th | 1.06 | 2.49 | 1.08 | 2.68 | 1.04 | 2.11 | 1.09 | 2.84 | 1.01 | 1.86 |
| 90th | 1.31 | 4.69 | 1.33 | 4.96 | 1.25 | 3.81 | 1.34 | 4.94 | 1.20 | 3.68 |

TABLE I: *NTR values at the specified percentile (10th, 50th, and 90th) for both sites and in different conditions (whole period of two years, working day, weekends, days, nights).*

the detectability threshold in the $[2, 10]$ Hz range. Nevertheless, already for the 50th percentile, we appreciate a $\simeq 12\%$ average loss in the SNR (Figure 11f) with 157 events ($\simeq 16\%$) below the SNR threshold. The 90th percentile shows, as expected, the worst performance with an average SNR loss $\simeq 37\%$ and 342 events ($\simeq 35\%$) with $SNR \leq 12$ in the considered bandwidth.

Considering Figure 5a, we expect that, having on average a few tenths of a second before an IMBH merge after leaving the $[2, 10]$ Hz range, a loss of SNR in this bandwidth may have an impact on the detectability and/or reconstruction of these events.

### B. Binary Neutron Stars

Figures 12 and 13 and Table III show the results obtained in the case of BNS signals. In total, we analyzed 1497 events of which 357 and 366 ($\simeq 24\%$) were already below the $SNR = 12$ threshold in the benchmark case for the Sardinia and EMR candidate sites, respectively. In general, the results are consistent with the IMBH case. The Sardinia candidate site has $\simeq 20\%$, $\simeq 21\%$ and $\simeq 25\%$ of events below threshold in the $[2, 10]$ Hz range for the 10th, 50th and 90th percentile case, respectively. These figures are on par, if not slightly better, with respect to the design case (Table III).

On the other hand, the EMR site shows less promising performances. The 10th percentile case equals the figure of the benchmark case, with $\simeq 22\%$ of events below the threshold in the frequency range of interest. The 50th and 90th percentile show the worst performance and loose $\simeq 32\%$ and $\simeq 54\%$ of events, respectively.

For what concerns the SNR ratios, the figures are consistent with the IMBH case and both sites show a gain/loss which is in line with what has been already discussed above.

### VII. CONCLUSIONS

We investigated the impact of site dependent ambient noise on the low frequency sensitivity of ET at the two sites candidate to host ET, Sardinia, in Italy, and the EMR region at the border between the Netherlands and Belgium. According to the currently available site characterization data, we focused on the impact of the seismic noise contribution to NN between 2 Hz and 10 Hz. Using the 10th, 50th and 90th percentile of the seismic spectra distributions covering two years at the two candidate sites, we inferred the impact on the ET sensitivity curve. We found that the Sardinia candidate site has the lowest impact on the design sensitivity. On the contrary, the local ambient noise recorded at EMR has a larger impact on the design sensitivity. This difference translates into an influence on the signal SNR of the astrophysical sources for which low frequency sensitivity plays a very important role, i.e. IMBH and BNS. Using the source parameters present in astrophysical catalogs obtained from population studies, we generated a set of waveforms and injected them into ET noise simulated according to the sensitivity curves derived from local ambient noise. SNR has then been calculated using the matched filter SNR. Comparing the resulting SNR distributions against the benchmark case obtained from the ET design sensitivity curve, we find that local ambient noise has a lower impact on the signal SNR in Sardinia, which is very close to design. The EMR site shows a significant SNR degradation, with respect to design.

Given the ET early warning requirements for BNS and the time to merger at 10 Hz of these signals, a significant degradation of the signal SNR may affect the ET early warning capabilities and hinder the possibility of extensive multimessenger observation campaigns for a number of events larger than expected. As we have found in our study, this is most likely to happen at EMR than Sardinia. Similarly, IMBH detection can also be affected.

In future, we will follow up this study to quantify the effect of local ambient noise on the source sky localization areas issued by early warnings using currently available detection pipelines. This will further expand the overview of the impact of ambient noise on the detectability of GW sources.

### ACKNOWLEDGMENTS

| | SNR/SNR$_{\text{DESIGN}}$ | | EVENTS WITH SNR $< 12$ | |
|---|---|---|---|---|
| Case | Sardinia | EMR | Sardinia | EMR |
| Design | n.a. | n.a. | 11% | 11% |
| 10th percentile | +6% | +3% | 9% | 11% |
| 50th percentile | +5% | −12% | 10% | 16% |
| 90th percentile | −2.5% | −37% | 11% | 35% |

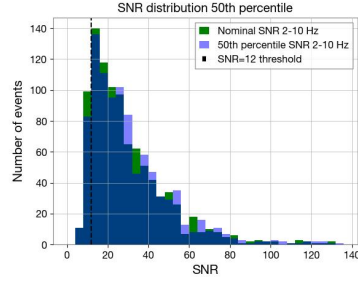TABLE II: *Summary of the SNR performance for the Sardinia and EMR candidate sites in the case of IMBH.*

| | SNR/SNR$_{\text{DESIGN}}$ | | EVENTS WITH SNR $< 12$ | |
|---|---|---|---|---|
| Case | Sardinia | EMR | Sardinia | EMR |
| Design | n.a. | n.a. | 24% | 24% |
| 10th percentile | +6% | +3% | 20% | 22% |
| 50th percentile | +5% | −12% | 21% | 32% |
| 90th percentile | −2.5% | −37% | 25% | 54% |

TABLE III: *Summary of the SNR performance for the Sardinia and EMR candidate sites in the case of BNS.*

[1] LIGO and Virgo Collaboration, Phys. Rev. X **9**, 031040 (2019).
[2] LVK Collaboration, Phys. Rev. X **11**, 021053 (2021).
[3] LVK Collaboration, arXiv:2111.03606 (2021).
[4] Virgo Collaboration, Classical and Quantum Gravity **32**, 024001 (2014).
[5] LIGO Scientific Collaboration, Class. Quant. Grav. **32**, 074001 (2015).
[6] KAGRA Collaboration, Nat. Astron. **3**, 35 (2019).
[7] M. Maggiore *et al.*, JCAP **2020**, 050 (2020).
[8] Branchesi *et al.*, JCAP **2023**, 068 (2023).
[9] Punturo *et al.*, Classical and Quantum Gravity **27**, 194002 (2010).
[10] ET Science Team, Class Quant. Grav. **27**, 194002 (2010).
[11] ET Science Team, **ET-0106C-10** (2011).
[12] ET Science Team, **ET-0028A-20** (2020).
[13] Hutt *et al.*, Bulletin of the Seismological Society of America **107**, 1402 (2017), https://pubs.geoscienceworld.org/ssa/bssa/article-pdf/107/3/1402/2641899/BSSA-2016187.1.pdf.
[14] Branchesi, Journal of Physics: Conference Series **718**, 022004 (2016).
[15] A. H. Nitz and T. D. Canton, The Astrophysical Journal Letters **917**, L27 (2021).
[16] Q. Hu and J. Veitch, The Astrophysical Journal Letters **958**, L43 (2023).
[17] LIGO and Virgo Collaboration, The Astrophysical Journal **848**, L12 (2017).
[18] M. Branchesi, "Gw170817: The dawn of multi-messenger astronomy including gravitational waves," in *Multiple Messengers and Challenges in Astroparticle Physics*, edited by R. Aloisio, E. Coccia, and F. Vissani (Springer International Publishing, Cham, 2018) pp. 489–497.
[19] Radice *et al.*, Astroph. Jour. Lett. **852**, L29.
[20] LSC Collaboration, Nature **551**, 85 (2017).
[21] F. Koliopanos, PoS **MULTIF2017**, 051 (2018).
[22] Mezcua, International Journal of Modern Physics D **26**, 1730021 (2017), https://doi.org/10.1142/S021827181730021X.
[23] Greene *et al.*, Ann. Rev. of Aston. Astroph. **58**, 257 (2020).
[24] Longuet-Higgins, Phil. Trans. R. Soc. Lond. **243**, 35 (1950).
[25] Ward and Crawford, Bulletin of the Seismological Society of America **56**, 793 (1966).
[26] Cessaro, Bull. Seism. Soc. Am. **84**, 142 (1994).
[27] Withers *et al.*, Bulletin of the Seismological Society of America **86**, 1507 (1996).
[28] Acernese *et al.*, Classical and Quantum Gravity **21**, S433 (2004).
[29] Coward *et al.*, Review of scientific instruments **76**, 044501 (2005).
[30] Virgo Collaboration, Journal of Physics Conference Series **32**, 80 (2006).
[31] Burtin *et al.*, Journal of Geophysical Research: Solid Earth **113** (2008).
[32] Anthony *et al.*, Geop. Res. Lett. **45**, 3436 (2018).
[33] Smith and Tape, JGR Solid Earth **124**, 11678 (2019).
[34] Dybing *et al.*, Geophysical Research Letters **42**, 765 (2019).
[35] Virgo Collaboration, Classical and Quantum Gravity **39**, 235009 (2022).
[36] Anthony *et al.*, Bulletin of the Seismological Society of America **112**, 646 (2022), https://pubs.geoscienceworld.org/ssa/bssa/article-pdf/112/2/646/5638811/bssa-2021176.1.pdf.
[37] Saccorotti *et al.*, Bull. Seis. Soc. Am. **101** (2011).
[38] Piccinini *et al.*, Scientific Reports **10**, 16487 (2020).
[39] Poli *et al.*, Scientific Reports **10**, 9404 (2020).
[40] Virgo Collaboration, Classical and Quantum Gravity **21**, S433 (2004).
[41] Virgo Collaboration, Journal of low frequency noise vibrations and active controls **30**, 63 (2011).
[42] Virgo Collaboration, arXiv:1108.1598 (2011).
[43] S. Koley, English*Sensor networks to measure environmental noise at gravitational wave detector sites*, Ph.D.
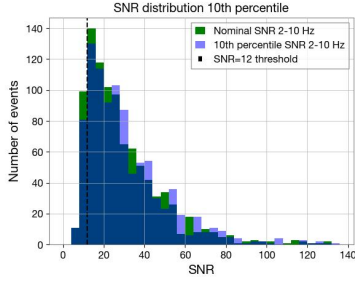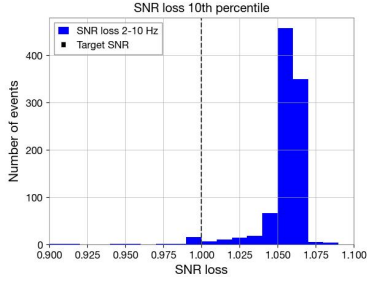
(a) *Sardinia Nominal SNR distribution (green) and SNR distribution using the 10th percentile ET sensitivity (blue).*
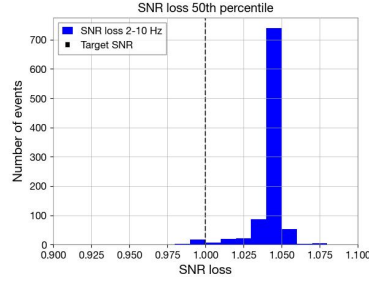
(b) *Sardinia nominal SNR distribution (green) and SNR distribution using the 50th percentile ET sensitivity (blue).*
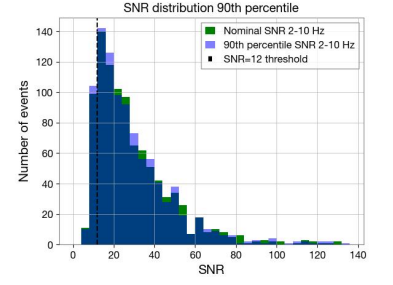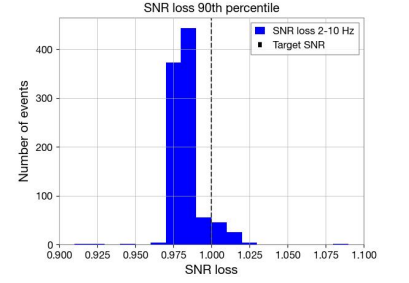
(c) *Sardinia nominal SNR distribution (green) and SNR distribution using the 90th percentile ET sensitivity (blue).*

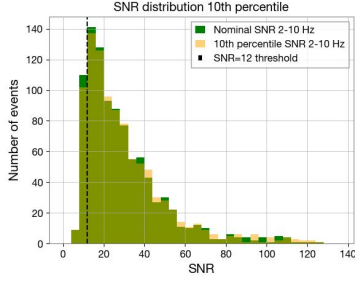(d) *Sardinia $SNR/SNR_{design}$ using the 10th percentile ET sensitivity.*
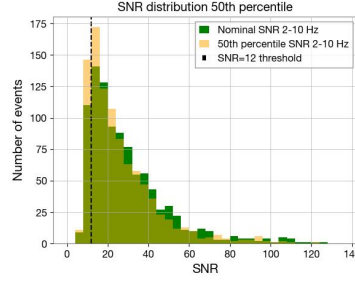
(e) *Sardinia $SNR/SNR_{design}$ using the 50th percentile ET sensitivity.*

(f) *Sardinia $SNR/SNR_{design}$ using the 90th percentile ET sensitivity.*

FIG. 10: IMBH SNR distributions for the Sardinia candidate site.

thesis, Vrije Universiteit Amsterdam (2020).

[44] Fiori *et al.*, in *Handbook of Gravitational Wave Astronomy* (Springer Singapore, Singapore, 2020) pp. 1–72.

[45] Accadia *et al.*, Classical and Quantum Gravity **27**, 194011 (2010).

[46] Martynov *et al.*, Phys. Rev. D **93**, 112004 (2016).

[47] Saulson, Physical Review D **30**, 732 (1984).

[48] Beccaria *et al.*, Classical and Quantum Gravity **15**, 3339 (1998).

[49] Harms, Living Reviews in Relativity **22** (2019), 10.1007/s41114-019-0022-2.

[50] Amann *et al.*, Review of Scientific Instruments **91**, 094504 (2020).

[51] Naticchioni *et al.*, Class. Quantum Grav. **31** (2014).

[52] Naticchioni *et al.*, J. Phys.: Conf. Ser. **1468** (2020).

[53] Di Giovanni *et al.*, Seis. Res. Lett. **92**, 352 (2021).

[54] Di Giovanni *et al.*, Geophysical Journal International **234**, 1943 (2023), https://academic.oup.com/gji/article-pdf/234/3/1943/50285042/ggad178.pdf.

[55] Allocca *et al.*, Eur. Phys. J. Plus. , 511 (2021).

[56] Saccorotti *et al.*, Eur. Phys. J. Plus **138**, 793 (2023).

[57] Koley *et al.*, First Break **37**, 83 (2019).

[58] M. Bader, S. Koley, J. van den Brand, X. Campman, H. J. Bulten, F. Linde, and B. Vink, Classical and Quantum Gravity **39**, 025009 (2022).

[59] S. Koley, M. Bader, J. van den Brand, X. Campman, H. J. Bulten, F. Linde, and B. Vink, Classical and Quantum Gravity **39**, 025008 (2022).

[60] Janssens *et al.*, PRD **137**, 102002 (2024).

[61] Harms *et al.*, Class. Quantum Grav. **36** (2019), 10.1088/1361-6382/ab28c1.

[62] W. Commons, "Sardinia relief location map," (2010), https://commons.wikimedia.org/wiki/File:Italy_Sardinia_relief_location_map.svg.

[63] W. Commons, "Netherlands relief location map," (2013), https://commons.wikimedia.org/wiki/File:Netherlands_relief_location_map.svg.

[64] W. Commons, "Europe relief location map," (2010), https://commons.wikimedia.org/wiki/File:Europe_relief_laea_location_map.jpg.

[65] LVK collaboration, AA **659**, A84 (2022).

[66] LIGO Scientific Collaboration and Virgo Collaboration (LIGO Scientific Collaboration and Virgo Collaboration), Phys. Rev. Lett. **125**, 101102 (2020).

[67] LVK Collaboration, AA **659**, A84 (2022).

[68] GRAVITY Collaboration *et al.*, AA **672**, A63 (2023).

[69] Maggiore, *Gravitational Waves - Volume 1* (Oxford University Press, New York, 2008).

[70] Husa *et al.*, Phys. Rev. D **93**, 044006 (2016).

[71] Khan *et al.*, Phys. Rev. D **93**, 044007 (2016).

[72] Dietrich *et al.*, Phys. Rev. D **100**, 044003 (2019).

[73] Miller *et al.*, Reviews of Geophysics **41** (2003), 10.1029/2003RG000124, https://doi.org/10.1029/2003RG000124.

[74] Harms *et al.*, The European Physical Journal Plus **137**, 687 (2022).

[75] Nitz *et al.*, "gwastro/pycbc: v2.3.3 release of pycbc," (2024).

[76] LVK Collaboration, "LVK Algorithm Library - LALSuite," Free software (GPL) (2018).

[77] Usman *et al.*, Classical and Quantum Gravity **33**, 215004 (2016).

[78] Peterson, *Observations and modeling of seismic background noise*, Tech. Rep. (US Geological Survey, 1993).

[79] Iacovelli *et al.*, "Bbh and bns source catalogs used for the coba science study," (2023), https://apps.et-gw.eu/tds/?r=18321.

[80] Mapelli *et al.*, Monthly Notices of the Royal Astronomical Society **511**, 5797 (2022), https://academic.oup.com/mnras/article-pdf/511/4/5797/42778203/stac422.pdf.

[81] Santoliquido *et al.*, Monthly Notices of the Royal Astronomical Society **502**, 4877 (2021), https://academic.oup.com/mnras/article-pdf/502/4/4877/36409570/stab280.pdf.
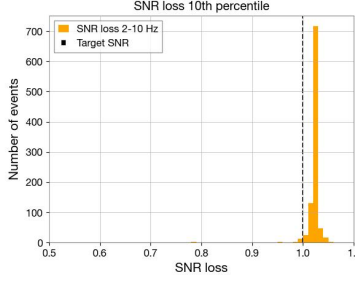
(a) *EMR Nominal SNR distribution (green) and SNR distribution using the 10th percentile ET sensitivity (blue).*
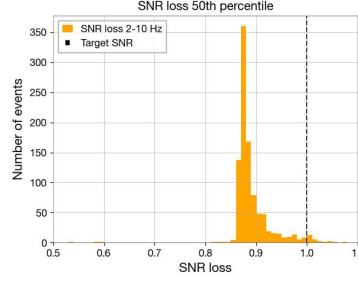
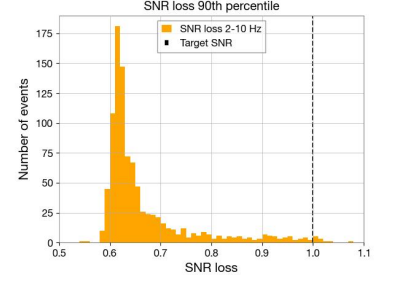(b) *EMR Nominal SNR distribution (green) and SNR distribution using the 50th percentile ET sensitivity (blue).*
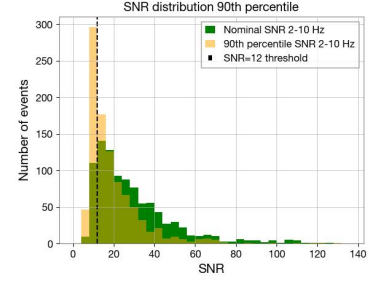
(c) *EMR Nominal SNR distribution (green) and SNR distribution using the 90th percentile ET sensitivity (blue).*

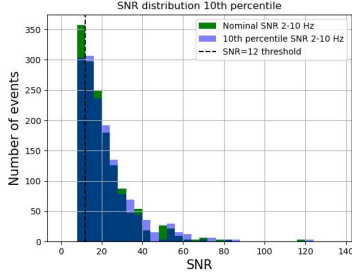(d) $SNR/SNR_{design}$ at EMR using the 10th percentile ET sensitivity.
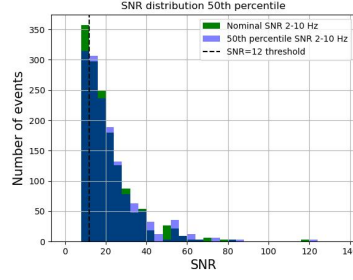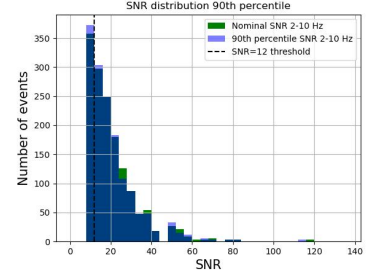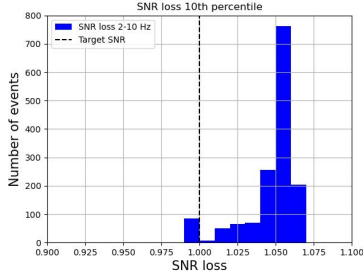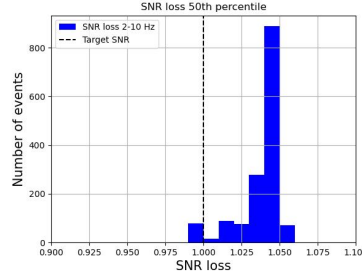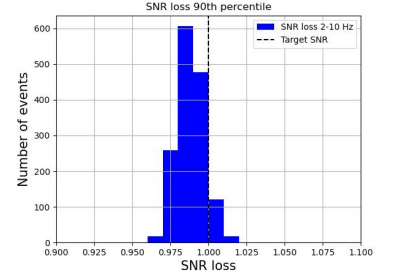
(e) $SNR/SNR_{design}$ at EMR using the 50th percentile ET sensitivity.

(f) $SNR/SNR_{design}$ at EMR using the 90th percentile ET sensitivity.

FIG. 11: IMBH SNR distributions for the EMR candidate site.

(a) *Sardinia Nominal SNR distribution (green) and SNR distribution using the 10th percentile ET sensitivity (blue).*

(b) *Sardinia nominal SNR distribution (green) and SNR distribution using the 50th percentile ET sensitivity (blue).*

(c) *Sardinia nominal SNR distribution (green) and SNR distribution using the 90th percentile ET sensitivity (blue).*

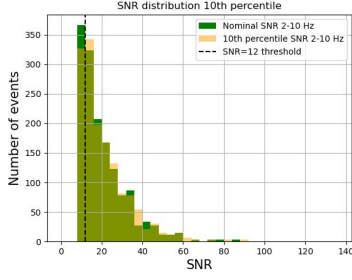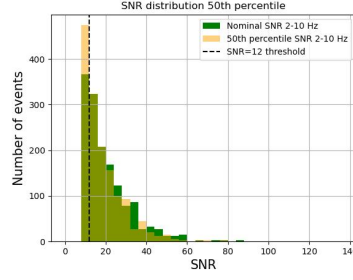(d) *Sardinia $SNR/SNR_{design}$ using the 10th percentile ET sensitivity.*

(e) *Sardinia $SNR/SNR_{design}$ using the 50th percentile ET sensitivity.*

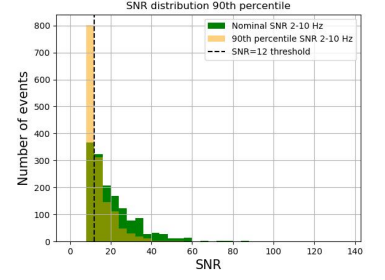(f) *Sardinia $SNR/SNR_{design}$ using the 90th percentile ET sensitivity.*

FIG. 12: BNS SNR distributions for the Sardinia candidate site.

(a) *EMR Nominal SNR distribution (green) and SNR distribution using the 10th percentile ET sensitivity (blue).*
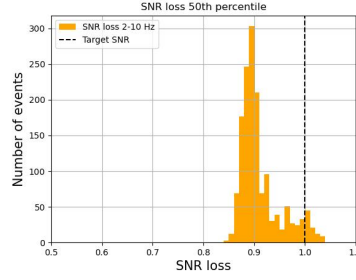
(b) *EMR Nominal SNR distribution (green) and SNR distribution using the 50th percentile ET sensitivity (blue).*
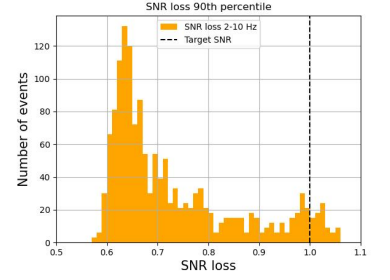
(c) *EMR Nominal SNR distribution (green) and SNR distribution using the 90th percentile ET sensitivity (blue).*
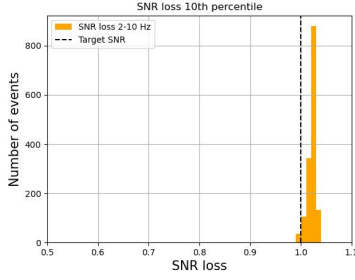
(d) $SNR/SNR_{design}$ *at EMR using the 10th percentile ET sensitivity.*

(e) $SNR/SNR_{design}$ *at EMR using the 50th percentile ET sensitivity.*

(f) $SNR/SNR_{design}$ *at EMR using the 90th percentile ET sensitivity.*

FIG. 13: IMBH SNR distributions for the EMR candidate site.